



Effects of upwelling duration and phytoplankton growth regime on dissolved oxygen levels in an idealized Iberian Peninsula upwelling system

João H. Bettencourt^{1*}, Vincent Rossi², Lionel Renault¹, Peter Haynes³, Yves Morel¹, Véronique Garçon¹

5 ¹LEGOS, University of Toulouse, CNES, CNRS, IRD, UPS, Toulouse 31400, France

²MIO (UM 110, UMR 7294), CNRS, Aix-Marseille Univ., Univ. Toulon, IRD, 13288, Marseille, France

³Department of Applied Mathematics and Theoretical Physics, University of Cambridge, England

*Correspondence to:

J. H. Bettencourt (joao.bettencourt@tecnico.ulisboa.pt)

10 Marine Environment Group

CENTEC - Centre for Marine Technology and Ocean Engineering

Instituto Superior Técnico (Pavilhão Central)

1049-001 Lisboa

Portugal

15 **Abstract.** We apply a coupled modelling system composed of a state-of-the-art hydrodynamical model and a low complexity biogeochemical model to an idealized Iberian Peninsula upwelling system to identify the main drivers of dissolved oxygen variability and to study its response to changes in the duration of the upwelling season and in phytoplankton growth regime. We find that the export of oxygenated waters by upwelling front turbulence is a major sink for nearshore dissolved oxygen. In our simulations of summer upwelling, when phytoplankton population is generally dominated by diatoms whose growth is
20 largely enhanced by nutrient input, net primary production and air-sea exchange compensate dissolved oxygen depletion by offshore export over the shelf. A shorter upwelling duration causes relaxation of upwelling winds and a decrease in offshore export, resulting in a slight increase of net dissolved oxygen enrichment in the coastal region as compared to longer upwelling durations. When phytoplankton is dominated by groups less sensitive to nutrient inputs, growth rates decrease and the coastal region becomes net heterotrophic. Together with the physical sink, this lowers the net oxygenation rate of coastal
25 waters, that remains positive only because of air-sea exchanges. These findings help disentangling the physical and biogeochemical controls of dissolved oxygen in upwelling systems and, together with projections of increased duration of upwelling seasons and phytoplankton community changes, suggest that the Iberian coastal upwelling region may become more vulnerable to hypoxia and deoxygenation.

1 Introduction

30 Marine hypoxia is an increasing global concern that is exacerbated by climate change, directly through warming-induced increase of stratification and decrease of oxygen solubility, and indirectly by changes in circulation and wind forcing (Levin, 2018). Declining dissolved oxygen (DO) in the world ocean and coastal realm impacts all marine life, from microbes to higher trophic levels (Breitburg et al., 2018), with consequences ranging from ecological adaptations and shifts (Gilly et al., 2013), changes of biogeochemical activity (Wright et al., 2012) to mass mortality events (Diaz and Rosenberg, 2008) and
35 biodiversity restructuring (Vaquer-Sunyer and Duarte, 2008).

Coastal waters are generally eutrophic and characterized by substantial planktonic productivity at the surface which favours oxygen consumption through remineralization of sinking organic matter, leading to low levels of DO in subsurface and near-bottom waters. Highly productive surface waters are typical of coastal upwelling regions and sustain socio-economically important ecosystems. Upwelling systems are thus especially sensitive to deoxygenation (Paulmier and Ruiz-Pino, 2009) and
40 to episodic hypoxia events with deleterious effects on marine life and human activities such as fisheries (Grantham et al., 2004; Hales et al., 2006; McClatchie et al. 2010; Roegner et al., 2011).



The western Iberian Peninsula Upwelling System (IPUS) is the northern branch of the Canary Upwelling System where the intra-annual variability of alongshore winds produce a seasonal upwelling/downwelling cycle (Wooster et al., 1976). In the summer and early fall, the Azores High migrates northward, causing a poleward alongshore wind that forces offshore Ekman
45 transport of surface waters and upwelling of subsurface waters, while downwelling prevails the rest of the year. Long-term studies of the seasonal upwelling in the IPUS have pointed to a weakening of upwelling winds over multidecadal time scales (Sousa et al., 2017), but simulations of future climate indicate an enhancement of the upwelling due to poleward migration of the Azores High and a lengthening of the upwelling season (Miranda et al., 2013; Rykaczewski et al., 2015; Sousa et al., 2017).

50 During the upwelling season, hydrographic and biogeochemical variability is primarily determined by the wind forcing that controls the inflow of offshore deep water masses onto the shelf (Alvarez-Salgado *et al.*, 1993). DO, in addition of being transported by the Ekman upwelling circulation, is also affected by the turbulent component of the circulation, characterized by sub/mesoscale fronts, filaments and eddies (Bettencourt et al., 2015; Capet et al., 2008; Chaigneau et al., 2009; Marchesiello et al., 2003; Montes et al., 2014; Vergara et al., 2016). These structures have a strong influence on the cross-
55 shore transport and on the vertical redistribution of biogeochemical tracers (Bettencourt et al., 2017; Combes et al., 2013; Gruber et al., 2011; Hernández-Carrasco et al., 2014; Nagai et al., 2015; Renault et al., 2016; Rossi et al., 2013).

From the biological perspective, the planktonic community structure can also affect DO in the water column, as this results from the balance between oxygen production by photo-autotrophs and respiration by both auto and heterotrophs. Changes in the community composition should lead to changes in the DO budget of the continental shelf. In the Iberian upwelling,
60 planktonic blooms tend to be dominated by large cells (micro-phytoplankton) such as diatoms (Moncoiffé et al., 2000; Rossi et al., 2013), that have lower respiration to photosynthesis ratios than dinoflagellates or cyanobacteria (López-Sandoval et al., 2014). Moreover, diatoms growth is thought to be positively correlated with the upwelling-driven nitrate inputs; in contrast, the growth of other planktonic groups can be insensitive to and even limited by newly-upwelled nitrates, especially when colimitation prevails or in the absence of necessary micro-nutrients. Thus, changes in the relative dominance of
65 functional groups in the community can lead to different autotrophy/heterotrophy regimes and total DO levels.

In this paper, we perform a process-oriented study coupling an idealized IPUS configuration of a hydrodynamic model with a low-complexity biogeochemical model centred on oxygen. We focus on the mechanisms of DO change to assess the relative role/importance of physical (upwelling duration) and biogeochemical (functional planktonic community) processes in setting DO levels and distribution. Previous studies have focused on the seasonal and climatological modelling of the
70 planktonic ecosystems and of dissolved oxygen (Marta-Almeida et al., 2012; Reboreda et al., 2014, 2015). Here, the spatio-temporal scales studied are shorter since we are interested in the variations and forcing mechanisms of DO levels in response to successive and short-lived upwelling pulses, commonly observed in the IPUS during the upwelling season. The coupled physical-biogeochemical model is presented in Sect. 2; our results are shown and analysed in Sect. 3. We then discuss our findings and conclude in Sect. 4.

75 2 Materials and methods

2.1 The coupled model

The idealized IPUS consist in a meridionally-oriented stretch of continental shelf with constant bathymetry and limited zonally by the coast and the open ocean (Fig. 1). The domain has 300 km of length and width, with a shelf width of 50 km, which is characteristic of the Iberian shelf at 41° N. The resolution of the spatial grid is 500 m, allowing the simulation of
80 summer upwelling seasons up to 90-day duration, with the associated upwelling front dynamics – meso and submesoscale vortices and filaments - within acceptable computing time limits.

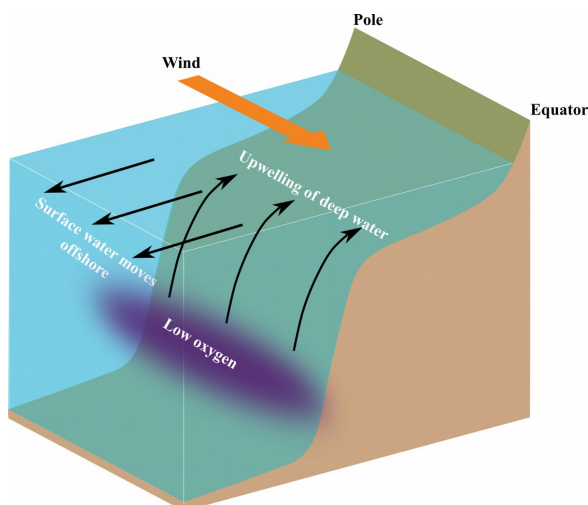


Figure 1. Idealized coastal upwelling configuration. The domain is periodic in the meridional (pole-equator) direction.

The physical-biogeochemical model couples the 3-dimensional Regional Ocean Modelling System ROMS (Shchepetkin, 2015; Shchepetkin and McWilliams, 2005), in its Coastal and Regional Ocean Community (CROCO) version (Debreu et al., 85 2012) to the low-complexity Oxygen-Phytoplankton-Zooplankton biogeochemical model of Petrovskii et al. (2017) and Sekerci and Petrovskii (2015), hereafter SP2015. Oxygen is used as the main model currency since it is central for the functioning of marine ecosystems (Breitburg et al., 1997, 2018). Oxygen is also at the heart of the photosynthesis and carbon fixation metabolic pathways for prokaryotic and eukaryotic algae, being a major electron acceptor (Mackey et al., 2008; Zehr and Kudela, 2009). and is needed for many biogeochemical reactions, including those involved in remineralization, that 90 constantly occur in the oceanic water column. On top of the oxygen that is produced and consumed within marine ecosystems, a considerable part of dissolved oxygen eventually become gaseous and is then exchanged at the ocean-atmosphere interface, contributing to the estimations that more than one half of atmospheric oxygen is produced in the ocean (Harris, 1986).

ROMS-CROCO is a hydrostatic primitive equation model, formulated in finite differences with time-splitting in the 95 barotropic (fast) mode and the baroclinic (slow) mode. It uses a terrain following vertical discretization in σ coordinates with 40 vertical levels. The prognostic variables are the horizontal barotropic and baroclinic momentum components, temperature and salinity. Free-surface displacement and vertical momentum are diagnostic variables. Horizontal advection of momentum and tracers is calculated from a 3rd order upstream biased scheme. Horizontal mixing is Laplacian, along iso- σ surfaces, with 100 diffusivity coefficients of $2 \text{ m}^2\text{s}^{-1}$ and $0.2 \text{ m}^2\text{s}^{-1}$ for momentum and tracers respectively. Vertical mixing uses the KPP scheme of Large *et al.* (1994). The model is initialized from rest; the initial temperature and salinity distributions are uniform in the horizontal and the vertical profiles are taken from the World Ocean Atlas 2013 climatology (Boyer et al., 2013). Initial fields of the biogeochemical tracers (O_2 , P and Z) are also horizontally homogeneous and their vertical profiles are obtained from a water column (e.g. 1-dimensional) model version of the O_2PZ model (not shown). The channel is periodic in the meridional 105 boundaries; the eastern boundary (coast) is modelled as a free-slip wall and the western one (open ocean) is open with radiative boundary conditions for momentum and tracers. Within the westernmost 50 km, a sponge layer is applied with increased horizontal viscosity of $200 \text{ m}^2\text{s}^{-1}$ and a nudging time-scale of 3 days in order to nudge all prognostic variables to their initial values over the offshore region. The bottom stress formulation is logarithmic with a roughness height of 0.01 m. The model is forced by a cyclic uniform wind field. To promote the destabilization of the upwelling front, we introduce a 110 small spatial perturbation to the wind field, whose amplitude is less than 1% of the total wind speed and with characteristic wavelengths of 10 km and 50 km in the alongshore and cross-shore directions, respectively.



In the coupled model, the time evolution of a tracer concentration C is given by:

$$\partial C/\partial t + u\partial C/\partial x + v\partial C/\partial y + w\partial C/\partial z = k(\partial^2 C/\partial x^2 + \partial^2 C/\partial y^2 + \partial^2 C/\partial z^2) + F_A + Q_C \quad (1)$$

- 115 where (u, v, w) is the 3D velocity field, k the tracer diffusivity, F_A is the air-sea oxygen exchange flux term (positive when the ocean receives oxygen) and Q_C is the source/sink term for the tracer C , here defined by the biogeochemical model O₂PZ (SP2015). It simulates seven biogeochemical reactions between the three compartments (Fig. 2) as follows:

$$Q_{O_2} = AJ(z)f([O_2])[P] - u_r([O_2], [P]) - v_r([O_2], [Z]) - m[O_2] \quad (2)$$

$$Q_P = l(N)g([O_2], [P]) - e([P], [Z]) - \sigma[P] \quad (3)$$

- 120 $Q_Z = \kappa([O_2])e([P], [Z]) - \mu[Z]$ (4)

In the source/sink term expression for DO (Eq. 2), the term $AJ(z)f([O_2])$ is the rate of O₂ production by photosynthesis and is modelled by a Monod parametrization $f([O_2]) = c_0/([O_2] + c_0)$, where c_0 is a half-saturation constant. The term $J(z) = 1 - \exp(\alpha PAR(z)/A)$ represents the light dependency of photosynthesis, with $\alpha = 30$ and the photosynthetically available radiation $PAR(z) = PAR(0) \exp(-k_w z)$, with $PAR(0) = 355.19 \text{ W/m}^2$ and $k_w = 0.04 \text{ m}^{-1}$.

- 125 We distinguish here the terms ‘photosynthesis’ from ‘carbon fixation’ (Behrenfeld et al., 2008). Indeed, ‘photosynthesis’ is the production of ATP and NADPH by the photosynthetic electron transport (PET) chain and these two products are referred to as ‘photosynthate’. By contrast, ‘carbon fixation’ refers to the use of photosynthate by the Calvin cycle to produce simple organic carbon products independently of light. SP2015 chose to highlight these two stages in their model formulation by decoupling carbon fixation from photosynthesis. The respiration by phytoplankton u_r is given by $u_r([O_2], [P]) = \delta[O_2][P]/([O_2] + c_2)$, where δ is the maximum per capita phytoplankton respiration rate and c_2 is the half saturation constant. Zooplankton respiration is similar: $v_r([O_2], [Z]) = v[O_2][Z]/([O_2] + c_3)$ and the constants v and c_3 have the same functions as in u_r . A Monod function is a logical formulation to have respiration depending on oxygen concentration since if the fluid environment becomes anoxic, then plankton cannot breathe so that respiration terms u_r and v_r vanish. The fourth term parametrizes bacterial respiration (oxygen loss due to natural depletion, e.g. remineralization).

- 135 In Eq. (3), phytoplankton growth $g([O_2], [P])$ is given by a linear growth term $\alpha([O_2])[P]$ minus intraspecific competition $\gamma[P]^2$, where γ is the intraspecific competition intensity. The per capita growth rate is a Monod function $\alpha([O_2]) = B[O_2]/([O_2] + c_1)$ where B is the maximum per capita growth rate in the large $[O_2]$ limit and c_1 is the half saturation constant. The $l(N)$ term is a Monod function $l(N) = k_i N(\rho)/(k_2 + N(\rho))$, where $N(\rho)$ is a parametrization of nutrient availability based on the nitrate-density (ρ) relationships measured during an oceanographic cruise which surveyed the IPUS during upwelling season
 140 (the 2007 MOUTON campaign, see also Rossi et al. 2010; 2013).

SP2015 used a formulation where high oxygen increases phytoplankton growth but limits oxygen production by photosynthesis. The Warburg effect (Turner, 1962) corresponds to the decrease of the photosynthesis rate at high oxygen concentrations so the choice of $f([O_2])$ where high $[O_2]$ limits $[O_2]$ production makes sense. Moreover oxygen stimulates photorespiration which reduces photosynthesis yield. As soon as a water molecule (H₂O) undergoes photolysis in the chloroplast of oxygenic photosynthetic organisms, O₂ as well as ATP (Adenosine TriPhosphate) are being produced through both photosystems I and II. The products of photosynthesis (ATP) then enters the Calvin cycle to convert carbon dioxide and other compounds into glucose, that is the food that autotrophs need to grow. As such, we can relate the growth term $\alpha([O_2])$ to $[O_2]$ with a Monod function so as high $[O_2]$ corresponds to high growth rate. The predation term is $e([P], [Z]) = \beta[P][Z]/([P] + h)$ where β is the maximum predation rate and h is the half saturation constant. Phytoplankton mortality is $\sigma[P]$. Regarding zooplankton, its feeding efficiency is a function of oxygen concentration $\kappa([O_2]) = \eta[O_2]^2/([O_2]^2 + c_4^2)$ where η is the maximum feeding efficiency and c_4 is the half-saturation constant. Zooplankton mortality is given by $\mu[Z]$.

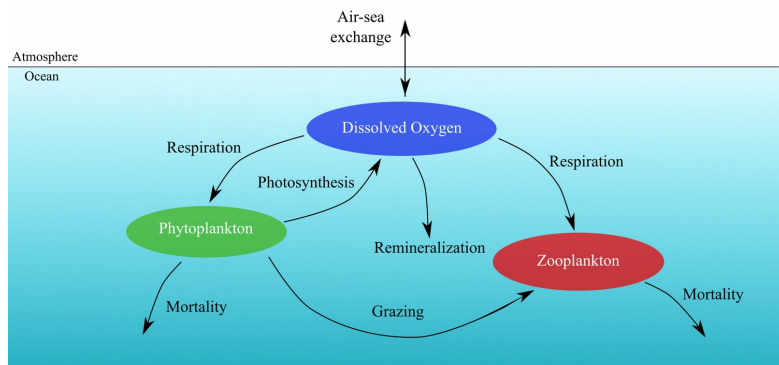


Figure 2. The Oxygen-Phytoplankton-Zooplankton model of SP2015, adapted to the oceanic environment.

The parameters of the O_2PZ model were adjusted so that its 0-D version (without advection or diffusion, see table A3) has a steady state at values representative of the IPUS (see Appendix A).
 155

2.2 Simulations

The coupled model is initialized at rest. Biogeochemical tracers are initialized from vertical profiles (Fig. 3(a)) obtained by a water column 1D model of the O_2PZ model that was run for long enough time to reach stable vertical distributions (not shown). Using these profiles instead of climatological initial conditions allows reducing the 3D coupled model drift (not shown). Initial temperature and salinity profiles (Fig. 3(b)) were taken from the World Ocean Atlas 2013 (WOA13, Boyer et al., 2013) data at 12°W and 41°N.
 160

Our set of simulations (Table 1) is designed to investigate the sensitivity of the coastal DO inventory to upwelling duration and community structure (diatom dominated or not). We choose the duration of upwelling-favourable wind instead of its magnitude as a control factor because it has been shown to be a better predictor of coastal hypoxia (Feng et al., 2012; Forrest et al., 2011; Zhang et al., 2018). Community structure is set through the growth regime of the primary producers (phytoplankton) with respect to nutrient input. Thus, a diatom dominated regime is simulated using enhanced growth rates due to nutrient input – the *(E)nhanced* runs - while a non-diatom dominated regime is simulated with growth rates *(N)utral* to and *(L)imited* by nutrient input. We test the sensitivity of our coupled system to the relative dominance of diatoms in the community as they have been suggested to decline over the long-term, being gradually replaced by dinoflagellates and cyanobacteria (Gregg et al., 2017).
 165
 170

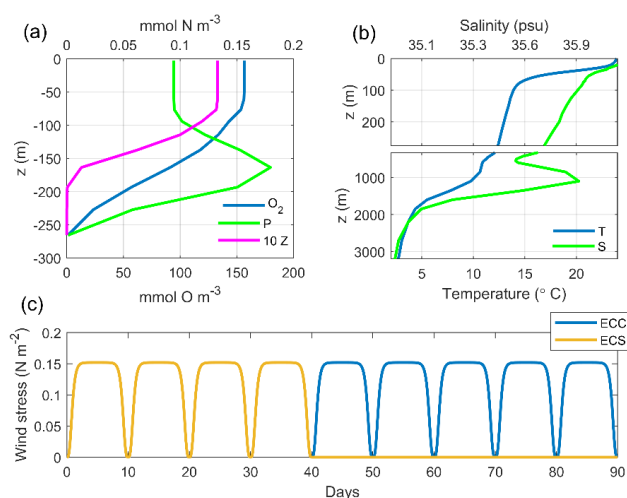
The effects of upwelling season length are studied by running two simulations where the number of upwelling favourable wind cycles are 4 and 9, maintaining a total simulation time of 90 days and considering a diatom dominated phytoplankton community. The wind profiles (Fig. 3(c)) are based on the cyclic wind pulses that are characteristic of the summer / early fall upwelling favourable conditions in the IPUS: 10-day pulses with maximum wind speed of 12 ms^{-1} (Rossi et al., 2013; Torres et al., 2003a).
 175

Table 1 Simulations. ECC is the reference simulation. All simulations are run for 90 days.

Simulation	P Growth (k_1, k_2)	Upwelling season
NCC	Neutral (1,0)	9 cycles
LCC	Limited (1,0.5)	9 cycles
ECC	Enhanced (2,0.5)	9 cycles
ECS	Enhanced (2,0.5)	4 cycles



In-situ observations of the IPUS, collected during the MOUTON 2007 campaign (Rossi et al., 2010; 2013), and compiled within the WOA13 (Boyer et al., 2013) are used not only to initialize but also to validate the outputs of our simulations. The
 180 ECC simulation used the wind forcing and phytoplankton growth regimes that most resemble the IPUS region and therefore was chosen as the reference simulation. We compared the full ranges of densities ρ , DO concentrations [O₂], and chlorophyll-a concentrations [Chl-a] of the reference simulation to all compiled measurements collected during the MOUTON campaign. We confirm that the coupled model, although of low complexity, reproduces relatively well the ρ -[O₂] and ρ -[Chl-a] relationships obtained from in-situ observations, despite a slight underestimation of [O₂] and [Chl-a] (Fig. 4).
 185 Note however that the cruise was specially designed to sample high coastal chlorophyll concentrations observed from satellite, so the dataset used in the comparison is biased towards high chlorophyll conditions.



190 **Figure 3. Initial conditions and wind forcing. (a) Initial profiles of O₂, P and Z. (b) Initial profiles of temperature (T) and salinity (S). (c) Wind forcing regimes; ECC: 9 wind cycles; ECS: 4 wind cycles.**

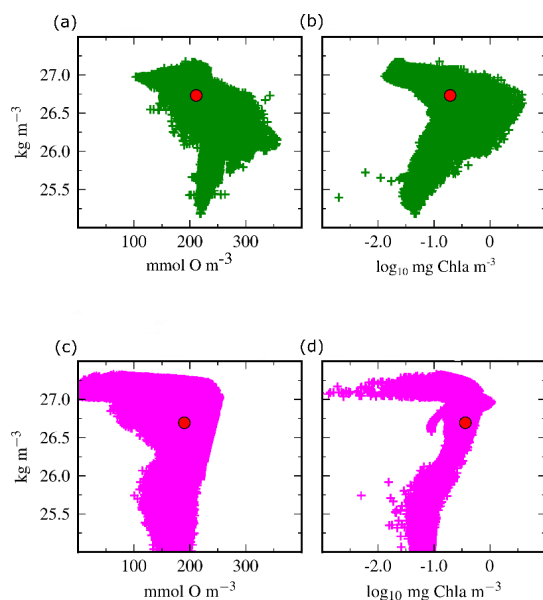




Figure 4. Validation of ECC simulation. a) Measured density vs. $[O_2]$; b) Measured density vs. $[Chl-a]$ (fluorescence as a proxy for $Chl-a$); c) Modeled density vs. $[O_2]$; d) Modeled density vs. $[Chl-a]$.

3. Results and discussion

195 3.1 Dissolved Oxygen in the Idealized IPUS

Our coupled model reproduces well the upwelling circulation and the typical biological responses. Indeed, the upwelling of nutrient-rich waters induced by the mean wind-driven circulation promotes the growth of phytoplankton, leading to increased oxygen production by photosynthesis and the subsequent enrichment of oxygen in shelf waters ($x < 80$ km, Fig. 5(a)), as compared with the lower $[O_2]$ found in offshore waters ($x > 80$ km). It also shows a low $[O_2]$ cell (~ 50 $mmol\ m^{-3}$), at the subsurface over the outer-shelf (centred at 40 km and 60 m depth) because of the upwelling of low O_2 waters, consistent with the shelf low $[O_2]$ cell (< 200 $\mu mol\ kg^{-1}$) measured during the MOUTON cruise (e.g. Rossi *et al.* 2013). Similarly, Gutknecht *et al.* (2013) in their modelling study of the Benguela upwelling region found a low $[O_2]$ plume for the climatological month of December at the shelf edge. For the Oregon coast, Hales *et al.* (2006) measured $[O_2]$ of 70-110 $mmol\ m^{-3}$ in upwelled water at the shelf break, about 200 $mmol\ m^{-3}$ less than at the surface, which is the same range of the vertical gradient simulated here.

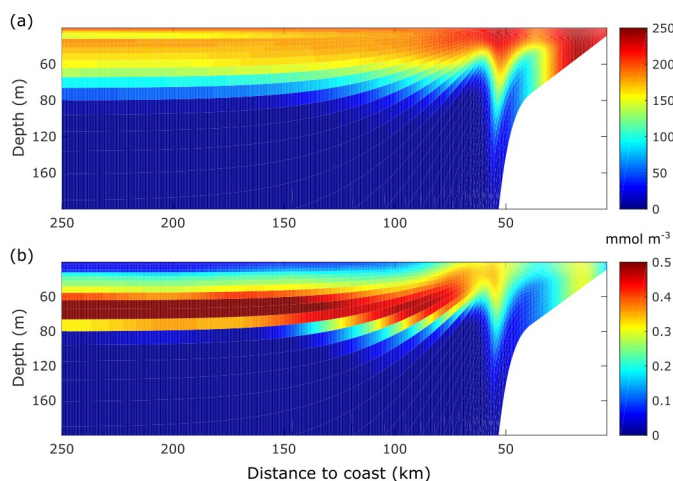


Figure 5. Mean $[O_2]$, $[P]$ fields of the ECC simulation. a) Time mean of along-shore averaged $[O_2]$ field. b) Time mean of along-shore averaged $[P]$ field. Time means are computed from day 20 to day 90.

The dynamics of the ECC simulation (Appendix B), are consistent with those documented by Durski and Allen (2005). A mean Ekman upwelling transport is established, moving subsurface waters upwards near the coast. The eddy induced circulation (Cerovečki *et al.*, 2009; Plumb and Ferrari, 2005) has the opposite sense to the mean circulation and is the strongest in the 50 to 100 km offshore range (Fig. B1). The result of the eddy induced onshore and downward circulation is mainly seen in the subduction of the oxygen rich waters just offshore of the shelf edge, as suggested by the spatial pattern of the eddy-stream-function (Fig. B1).

The spatial coincidence between the high $[O_2]$ and high phytoplankton concentration $[P]$ near the coast (Fig. 5) reflects O_2 enrichment caused by photosynthetic production (see Sect. 3.2 for a budget analysis). Since oxygen limits phytoplankton growth in our model, the low $[O_2]$ cell in the coast causes a matching low $[P]$ cell at the same location. Further offshore, subsurface $[P]$ and $[O_2]$ decrease as phytoplankton growth is limited by the lack of nutrients in the euphotic zone.

The subsurface $[P]$ maximum between 60 and 80 meters depth results from the trade-off between sufficient oxygen, light levels and nutrients availability. Consequently, the enhanced phytoplankton growth rate due to nutrients appears to



compensate for the low oxygen levels, thus promoting phytoplankton growth. Moreover, the low $[O_2]$ will maintain the zooplankton stocks at low levels, thus constraining the grazing pressure of zooplankton on phytoplankton.

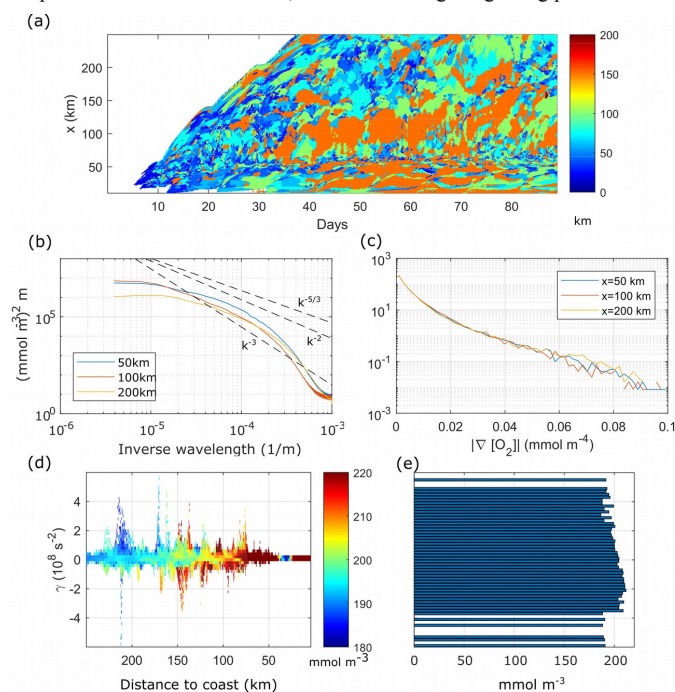


Figure 6. a) Peak wavelength of surface $[O_2]$ alongshore wavenumber spectrum as a function of time and offshore shore distance. b) Time mean surface $[O_2]$ alongshore wavenumber spectrum at $x=50$ km, 100 km, and 200 km offshore. $[O_2]$ spectra computed from anomalies with respect to alongshore mean. c) PDF of time mean surface $[O_2]$ gradient norm at $x=50$ km, 100 km, and 200 km. d) Instantaneous distribution of surface $[O_2]$ by x and γ at day 65. e) Distribution of x -averaged $[O_2]$ by γ at day 65. Time mean taken from day 20 to day 90.

230 The dominant length-scales, i.e. the inverse of the wave number where the alongshore $[O_2]$ anomaly field spectrum has a maximum, vary with time and distance to coast (Fig. 6(a)). After day 30, between 50 and 150 km offshore we observe the emergence of dominant length scales of 150 km in an intermittent fashion, in a process that agrees with previous studies of the growth and decay of large mesoscale structures in coastal upwelling systems (Durski and Allen, 2005).

Slopes of time averaged spectra of alongshore $[O_2]$ anomalies at three offshore locations (Fig. 6(b)) show, however, that submesoscale has also a marked effect on the $[O_2]$ field. All spectra are shallower than the k^{-3} slope of geostrophic turbulence (Charney, 1971), implying that the submesoscale is prominent in our simulations (Capet et al., 2008). The spectrum at $x=50$ km is the shallowest and the closest to the $k^{-5/3}$ slope in the range $8 \cdot 10^{-4} < k < 10^{-4}$. In the lower k range ($k < 10^{-5}$), the spectra at 50 and 100 km have higher energy than the spectrum at 200 km, as the dominant length-scale plot shows the largest dominant length-scales in the 50-150 km cross-shore region.

240 The Probability Density Function (PDF) of the $[O_2]$ gradient norm (Fig. 6(c)) has a heavy tail distribution, associated with intermittency (Capet et al., 2008; Castaing et al., 1990). The existence of long tails in all PDF's indicates that sharp $[O_2]$ gradients are ubiquitous in the channel.

Turbulence redistributes oxygen through fronts and filaments (strain-dominated regions) as well as vortices (rotation-dominated regions). To analyse this process, we use the Okubo-Weiss criterion γ , which separates turbulent velocity fields in strain-dominated ($\gamma > 0$) and rotation-dominated ($\gamma < 0$) regions. More specifically, we compute the daily average surface $[O_2]$ for each γ and binned shore distance x .



For day 65, the $[O_2]$ distribution by (γ, x) (Fig. 6(d)) reproduces the cross-shore $[O_2]$ gradient of coastal elevated $[O_2]$ and lower offshore $[O_2]$ (the background gradient, see also Fig. 5 (a)), in the range $\gamma \sim 0$. Deviations from this background gradient are found along the cross-shore direction, as we move to larger $|\gamma|$, implying that $[O_2]$ anomalies with respect to the mean surface field are mainly found in filaments and vortices. Since the highest $[O_2]$ levels are found in the shelf region, due to photosynthetic production, their presence further offshore strongly suggests offshore export by turbulent structures. We emphasize that offshore transport of $[O_2]$ rich water results in a net loss of O_2 for the continental shelf region.

The $[O_2]$ anomalies found offshore in positive and negative γ regions highlight the transport and dispersion of O_2 by sub/mesoscale structures from the shelf to the open ocean. We find that although the mean $[O_2]$ as a function of γ (averaged over x in each γ bin) remains at $\sim 200 \text{ mmol m}^{-3}$ (Fig. 6 (e)), the $[O_2]$ distribution is biased toward negative γ , as found by Combes *et al.* (2013) for tracers in the California current. Our results are also in line with those of Lovecchio *et al.* (2017) that demonstrate the importance of mesoscale processes for the zonal advection of tracers, with a key role of eddies, especially offshore the upwelling front.

The relative importance of the physical versus the biological processes in controlling coastal oxygen dynamics was analysed in terms of the volume averaged rate of change of DO due to physics (advection and mixing), biology (photosynthesis, community respiration and remineralization) and air-sea fluxes within a shelf control volume (from the coast to 50 km offshore and from the surface to 140 m depth) and averaged from day 20 to 90. The net enrichment rate, accounting for the physical and biological forcing, is positive ($2.26 \text{ mmol m}^{-3} \text{ d}^{-1}$) and so, over time, the coastal oxygen inventory increases. DO concentrations are increased by biogeochemical processes at a rate of $4.27 \text{ mmol m}^{-3} \text{ d}^{-1}$ and by air-sea exchange ($3.41 \text{ mmol m}^{-3} \text{ d}^{-1}$) but are limited by physical processes that remove O_2 from the coastal region ($-5.42 \text{ mmol m}^{-3} \text{ d}^{-1}$) through lateral advection.

3.2 Sensitivity of dissolved oxygen to upwelling duration and phytoplankton growth regimes

The reference simulation (ECC) has shown three major features: the appearance of sub-surface low $[O_2]$ cells because of the upwelling of O_2 poor waters, the O_2 enrichment of surface levels, and the appearance of an $[O_2]$ gradient between the biologically-mediated enrichment at the inner shelf and the depleted offshore region. This gradient is, on one hand maintained by the upwelling circulation and, on the other hand, smoothed out by the cross-shore transport of O_2 by small-scale vortices and filaments. These effects are driven by the wind regime, that controls the upwelling dynamics and instabilities, and by phytoplankton growth rate, which in turn affects phytoplankton concentrations. We now look at the sensitivity of the coupled model to these two drivers.

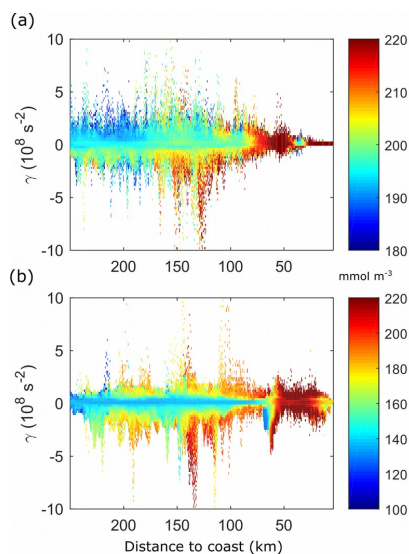
The continuous development of filaments and vortices in the ECC run maintains the offshore transport of dissolved oxygen (Fig. 7 (a)). The wind shutdown in the ECS run causes a gradual decrease of turbulence which implies a diminution of the $[O_2]$ redistribution by the cross-shore export physical processes, resulting in the creation of a sharper boundary between the oxygen-rich coastal waters and the depleted open ocean (offshore the upwelling front, Fig. 7 (b)).

The phytoplankton growth regime impacts the mean $[O_2]$ distribution since nutrient neutrality (NCC) or limitation (LCC) results in the decrease of $[O_2]$, when compared with the ECC run. The largest difference between the NCC and the ECC simulations (Fig. 8(a)), are observed in the coastal region, with maximum deviations from the ECC run up to 100 mmol m^{-3} . Offshore of the front, on the other hand, we find an increase of $[O_2]$ with respect to the ECC run, with the difference reaching $\sim 50 \text{ mmol m}^{-3}$ at $x=250 \text{ km}$. This positive difference is due to the absence of nutrient limitation, so that phytoplankton growth and oxygen production persist in the nutrient depleted surface levels.

The difference between the LCC and ECC cases (Fig. 8(b)) is also the highest in the shelf region, slightly above 100 mmol m^{-3} . Offshore of the front ($x > 50 \text{ km}$), the difference reduces to less than 50 mmol m^{-3} , above 80 m depth, vanishing below

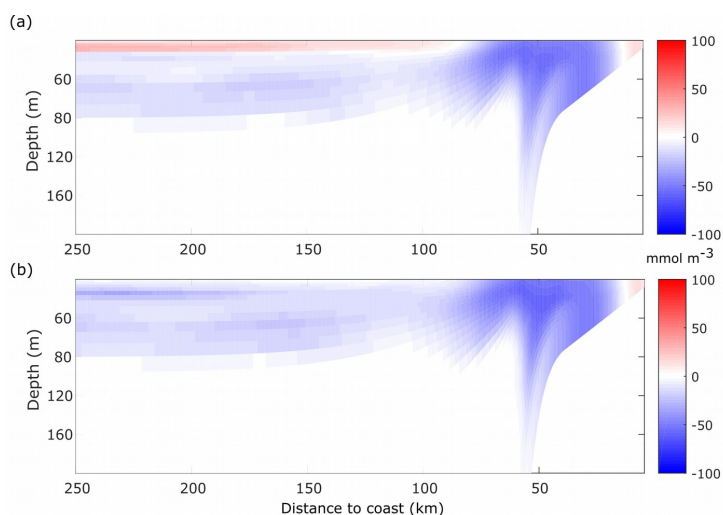


this depth. In both cases, there is a signature of the low $[O_2]$ upwelling over the slope and shelf edge and the eddy-induced subduction just offshore of the front ($x=50$ km).



290

Figure 7. Time mean distribution of $[O_2]$ by x and γ . (a) ECC. (b) ECS. Time mean taken from day 20 to 90.



295

Figure 8. Difference in time mean dissolved oxygen with respect to the ECC run. (a) NCC. (b) LCC. Time mean taken from day 20 to 90

300

When analysing O_2 budgets in the coastal control volume, from shore to 50 km offshore and from surface to 200 m of depth, the short upwelling duration simulation (ECS) results in a slight increase of the shelf $[O_2]$ temporal mean net rate of change by 6% with respect to the ECC simulation (2.26 to 2.40 $mmol\ m^{-3}\ d^{-1}$, Figure 9(a)). Although for ECS every term in the oxygen mean budget is smaller than for ECC, the physical sink decrease is slightly higher than the combined decrease in biological source and sink (Q_{O_2}) and air-sea exchange.



The changes in physical sink also occur faster than those in the biological terms. The wind cessation at day 40 causes an immediate decrease in the physical term (Fig. 9(b), lower panel) while only after day 70 can we observe a significant difference between the biological source/sink terms of both ECC and ECS simulations.

305 Changes in the phytoplankton growth regime modify the physical-biological balance of oxygen in the coastal control volume. The coastal region is net autotrophic ($Q_{O_2} > 0$) for ECC ($Q_{O_2} = 4.27 \text{ mmol m}^{-3} \text{ d}^{-1}$) and ECS ($Q_{O_2} = 3.99 \text{ mmol m}^{-3} \text{ d}^{-1}$) but becomes slightly net heterotrophic ($Q_{O_2} < 0$) when the phytoplankton growth becomes neutral to (NCC, $Q_{O_2} = -0.11 \text{ mmol m}^{-3} \text{ d}^{-1}$) or limited by (LCC, $Q_{O_2} = -0.35 \text{ mmol m}^{-3} \text{ d}^{-1}$) nutrients (Fig. 9(a)). This modifies the $[O_2]$ gradients and the $[O_2]$ lateral advective fluxes and, as a result, the rate of oxygen loss through lateral advection decreases by about 15% for NCC and LCC, with respect to ECC. The air-sea exchange of O_2 is also affected by the growth regime changes, as lower $[O_2]$ will result in increased fluxes.

310

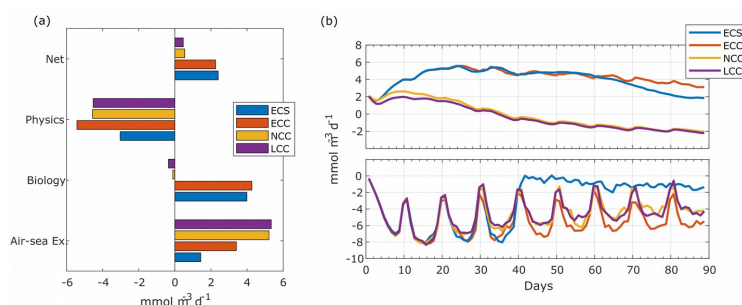


Figure 9. Dissolved Oxygen budgets in the coastal control volume. (a) Time mean rate of change of dissolved oxygen. Net value is the sum of Physical, Biological and Air-sea exchange source/sink terms. Physical terms are the sum of cross-shore, alongshore and vertical advectons as well as horizontal and vertical mixing. Biological term is oxygen photosynthetic production minus community respiration. Time mean taken from day 20 to 90. (b) Time series of average rate of change of dissolved oxygen in the coastal control volume due to biology (top) and physics (bottom).

315

320 Overall, the phytoplankton growth regime has a stronger impact than the wind regime in the DO inventory in the shelf control volume. The NCC and LCC cases result in net rates of change of dissolved oxygen that are 75%-80% lower than in the reference case.

4 General discussion and conclusions

We built a coupled physical-biogeochemical model of an idealized seasonal coastal upwelling to study the effect of the upwelling season length and phytoplankton community structure on dissolved oxygen inventory. While we used data from the Iberian Peninsula upwelling to initialize and validate the range of values simulated by our model, our idealized configuration allows to draw general conclusions about the mechanisms governing the dissolved oxygen levels over the continental shelf. When compared to measurements, our model reproduces well the O_2 -density relationship as well as upwelling of oxygen-poor waters onto the shelf and the offshore transport of oxygen due to filaments and vortices. While the addition of air-sea exchange processes as well as our novel nutrient/density parametrization have probably contributed largely to simulate such realistic outputs despite the simple biogeochemical formulation, the coupled system could be further improved. One probably important task, that we keep for future studies, is to include realist subsurface O_2 inputs from oceanic currents, as it has been shown to control largely O_2 dynamics over the shelf [Montes et al., 2014; Reboreda et al., 2015].

325

330



335 Although there is a clear separation of coastal waters with high $[O_2]$ and offshore waters with low $[O_2]$, the turbulent lateral
transport of high $[O_2]$ water disrupts this picture, as oxygen-rich upwelling filaments and vortices generated at the front and
then travel offshore. This creates a sink of dissolved oxygen on the shelf that must be compensated by photosynthetic
production and air-sea fluxes. In our reference simulation, with repeated upwelling wind cycle, the net $[O_2]$ rate of change
was positive, owing to the predominance of the photosynthetic oxygen production and air-sea fluxes over the lateral
340 transport of oxygen, that acts to remove it from the shelf region. When considering a shorter upwelling season (the ECS case
with four 10-day upwelling wind cycles followed by wind cessation) reinforces somewhat the oxygen enrichment trend.
When phytoplankton community is dominated by groups that show nutrient limitation or neutral growth (LCC and NCC
cases), the biological source weakens and the shelf becomes net heterotrophic. The physical sink is also affected, producing a
weaker loss of dissolved oxygen in the coastal upwelling. Air-sea exchange then maintains the (much lower) net oxygen
345 enrichment trend

Our findings that the oxygen inventory net rate of change is inversely proportional to the duration of upwelling season is
consistent with other studies (Adams et al., 2013; Siedlecki et al., 2015; Zhang et al., 2018) and, as the upwelling season
duration in the IPUS is thought to increase in the future (Miranda et al., 2013; Wang et al., 2015), it suggests increased
vulnerability of coastal regions to hypoxia and long-term deoxygenation. The result of lower phytoplankton growth rates
350 driving the shelf region from autotrophy to heterotrophy also points to an increased risk of loss of dissolved oxygen if trends
for community shifts towards smaller or less efficient phytoplankton (Gomes et al., 2014; Gregg et al., 2017; Head and
Pepin, 2010; Zhai et al., 2013) are specifically confirmed for the IPUS.

Code/Data availability

Simulated data and computer codes are available upon request.

355 Appendix A. Determination of O_2 PZ model parameters.

The biogeochemical component of the 3D coupled model (Eqs. (1), (2)-(4)) is a system of ODE's that computes the local
time evolution of $[O_2]$, $[P]$ and $[Z]$. The ODE system accounts for the processes that move O_2 , P and Z between different
reservoirs. Each ODE of the model then expresses the input and output of the species from the specific reservoir. The
dynamical properties the ODE's will therefore influence the global behaviour of the coupled physical-biogeochemical
360 model. When using coupled models such as (1), it is good practice to work in the vicinity of a known co-existence stable
fixed point, i.e a solution $X^+ = ([O_2]^+, [P]^+, [Z]^+) \neq (0,0,0)$ to Eqs. (2)-(4) that doesn't change with time and attracts nearby
system trajectories. This guarantees that, when removing the advection and diffusion terms, the system will evolve to a
constant state whose properties are already established (e.g. positive concentrations). The fixed points of the O_2 PZ system
are the states X^+ where

$$365 \quad d[O_2]^+/dt = d[P]^+/dt = d[Z]^+/dt = 0 \quad (A1)$$

Since the system is nonlinear, solution of Eq. (A1) is not straightforward and approximate methods are then a good choice.
Since the model will be used to study O_2 dynamics in coastal upwelling systems in the Iberian Peninsula western shelf/slope,
it is logical that the model uses initial conditions that are characteristic of this region. The characteristic state $X^w = ([O_2]^w,$
 $[P]^w, [Z]^w)$ may be taken from climatological dataset, in-situ observations, remotely-sensed data, etc. as long as it is
370 representative of the actual values of $([O_2], [P], [Z])$ in that region. Regarding the position of X^w in the state space, a simple
proposition is that X^w is close to a coexistence steady state X^0 . This means that, if the model is initialized at X^w it will
converge to X^0 and will not evolve to an extinction state or other steady states with unrealistic or uncharacteristic values of



375 $([O_2],[P],[Z])$ for the region. This is the approach adopted here to study the fixed points and determine the values of the parameters of the system and we adopt the characteristic values shown in Table A1 for the Iberian Peninsula upwelling.

Table A1. Characteristics values of O_2 , P and Z for the western Iberian Peninsula.

Variable	Value
$[O_2]^w$	0.255 mmol O L ⁻¹
$[P]^w$	0.063 mmol O m ⁻³
$[Z]^w$	0.017 mmol O m ⁻³

380 The concentration of DO is taken from the climatological mean at 12°W, 41° N and 10 m depth. The phytoplankton concentration is obtained from ocean color images of chlorophyll a in the west Iberian shelf at approximately the same position of the DO reading, after converting it to nitrogen concentration using a ratio of 1.59 between Chl a and nitrogen content (Montes et al., 2014). Finally, the zooplankton concentration is found by using a phytoplankton to zooplankton ratio of 3.6, taken from SP2015 for the case of a stable co-existence state of the nondimensional model. For some parameters we adopt the values that are used elsewhere in the literature. To find the most adequate values of the remaining parameters, we search for the parameters that make possible the propositions above regarding the stable nature of X^w . To proceed, we consider first the system obtained by setting $[Z] = 0$.

385 Applying the fixed point condition (A1), we obtain two equations relating $[P]$ and $[O_2]$:

$$P_1([O_2]) = (m[O_2]([O_2]+c_0))/([O_2]+c_2)/(Ac_0c_2+(A-\delta)c_0[O_2]-\delta[O_2]^2) \quad (A2)$$

$$P_2([O_2]) = 1/\gamma(Bc/([O_2]+c_1) - \sigma) \quad (A3)$$

390 The fixed points of the system are given by $P_1 = P_2$ in the positive quadrant of the $([O_2], [P]; [Z] = 0)$ plane, in addition to the extinction steady state. Explicit computation of the fixed points is not possible for the $[O_2]$ - $[P]$ - $[Z]$ system, but we can derive relationships of the form $[Z] = f([O_2],[P])$ that satisfy (A1) from the oxygen and phytoplankton equations, as follows:

$$Z_1([O_2],[P]) = ([O_2] + c_3)/\nu[O_2] ((Ac_0[P])/([O_2]+c_0)-(\delta[O_2][P])/([O_2]+c_2)-m[O_2]) \quad (A4)$$

$$Z_2([O_2],[P]) = ([P]+h)/\beta[P] (B[O_2][P]/([O_2]+c_1)-\gamma[P]^2-\sigma[P]) \quad (A5)$$

395 The zooplankton equation does not produce a similar relationship. Instead, analytical manipulation of it let us derive the following expression:

$$[Z]=0 \quad [P]=P_z=hM([O_2])/(1-M([O_2])), \quad (A6)$$

where $M([O_2])=\mu/\beta (([O_2]^2+c_4^2)/\eta[O_2]^2)$. The fixed points of the $[O_2]$ - $[P]$ - $[Z]$ system are the loci of intersection of Eqs. (A4)-(A6) in the $([O_2] > 0; [P] > 0; [Z] > 0)$ octant. Note that the terms in parenthesis in Eqs. (A4), (A5) are the equations of the oxygen-phytoplankton system. In fact, if $[Z] = 0$, Eqs. (A4), (A5) reduce to Eqs. (A2), (A3), as expected.

400 There are 11 parameters that relate O_2 with phytoplankton and zooplankton. It is a considerable amount of free parameters to handle. To constrain the choice of values for this set of parameters, making it easier to tune the model, we introduce the following three assumptions, regarding the model behaviour at X^w :

1. At X^w , zooplankton growth should not be hampered by the value of $[O_2]^w$. This requires that the feeding efficiency term is at or near its maximum h .
- 405 2. At X^w , the phytoplankton growth rate should be near or at its maximum value of B .
3. At X^w , phytoplankton O_2 production rate is significantly larger than O_2 respiration rate.

These assumptions are adopted to facilitate a co-existence state at X^w , by not limiting the ability of zooplankton to feed on phytoplankton and at the same time by facilitating phytoplankton growth to feed zooplankton and to produce O_2 in a greater amount than it respire.

410 Since the position of the fixed points of the system is given by the intersections of the isoclines Z_1 , Z_2 and P_z , they should intersect at or near $([O_2]^w; [P]^w)$ and the fixed point at the intersection should be stable. This can be achieved by changing the parameters of the system in order to move the isoclines in phase-space, and at the same time check the sign of the real part of



the eigenvalues of the system Jacobian matrix at the intersection to identify the stability type of the fixed point. In Fig. A1, we plot the three isoclines in the plane $v = 0$ for different values of the parameters A, B and h. It shows how the isoclines change with the changing parameters. Since both Z_1 and Z_2 depend on $[Z]$, we must look at the 3D phase space to see where the isoclines intersect (Fig. A2).

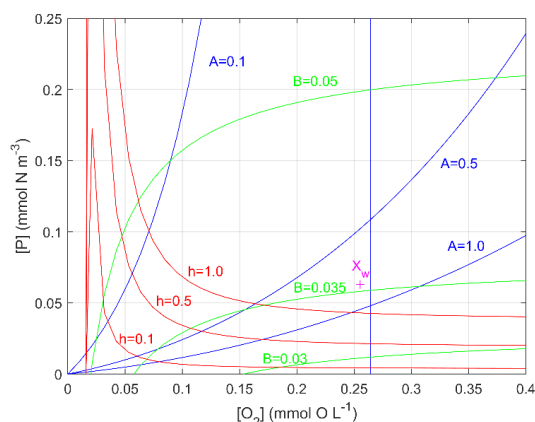
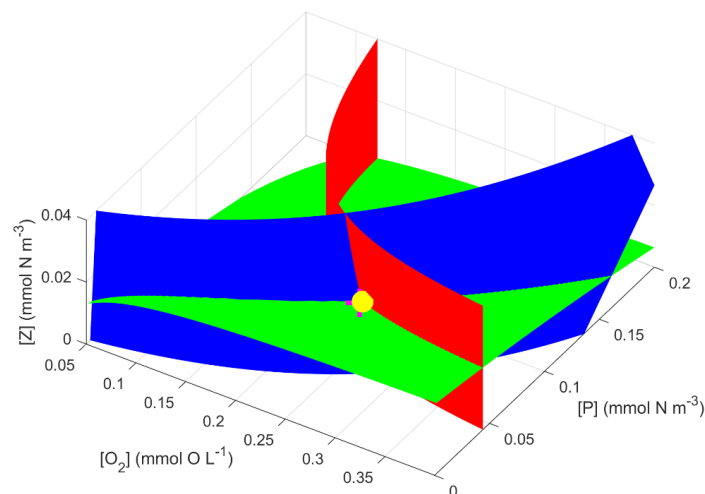


Figure A1. Isoclines of the $[O_2]$ - $[P]$ system for selected values of A, B and h. Blue: P_1 ; Green: P_2 ; Red: P_z .



420

Figure A2. Isoclines of the $[O_2]$ - $[P]$ - $[Z]$ system. Blue: Z_1 ; Green: Z_2 ; Red: P_z . Yellow: X^0 . To build this figure, we set up a grid of $([O_2]_i; [P]_j)$; $i, j = 1; \dots; N$ values and plotted $Z_1(i; j)$ and $Z_2(i; j)$ from Eqs. (A4) and (A5). The P_z isocline is different since it does not depend on $[Z]$, so we computed $P_z(i) = hM(c_i) / (I - M(c_i))$ with M defined in the text, and extended it vertically up.

To find the intersection point, that corresponds to the co-existence steady state X^0 , we computed the distance $d_{12}(i; j) = Z_2(i; j) - Z_1(i; j)$, so that the intersection $Z_2 = Z_1$ is given by $d_{12} = 0$. The zeros of d_{12} were identified approximately by choosing, for each $[O_2]_i$, the value of $[P]_j$ that minimized $d_{12}(i; j)$. To find X^0 , we used a similar procedure to find the point where this line intersects P_z . This procedure is approximate, and its accuracy varies with N. By performing tests for several N, we found that N = 300 gave enough accuracy. By varying A, B and h, the intersection (X^0) can be made to approach X^w . Although other parameters may be varied instead of these three, we found that these are the ones whose variations are easier to judge in terms of displacement of the isoclines. We note that, of the three, only h is one of the "fixed" parameters that was found in

430



the literature, but since it is quite easy to move P_z by changing its value, we decided to use it as a tuning parameter. The result of this exercise is that the co-existence fixed point X^0 is located near X^w , with coordinates shown in Table 2 and is a stable spiral point with eigenvalues of the Jacobian $\lambda_1 = -0.0847$ and $\lambda_{2,3} = -0.0009 \pm 0.0221i$.

435 **Table A2. Coordinates of the co-existence fixed point X^0 .**

Variable	Value
$[O_2]^0$	0.261 mmol O L ⁻¹
$[P]^0$	0.052 mmol N m ⁻³
$[Z]^0$	0.018 mmol N m ⁻³

Table A3. Parameters of the 0-D SP2015 biogeochemical model.

Parameter	Value	Units	Description
A	0.54	d ⁻¹	Environmental effects in rate of O ₂ production inside phytoplankton cells.
c_0	0.255	mmol O L ⁻¹	Half-saturation constant for O ₂ production.
δ	0.2	d ⁻¹	Maximum per capita phytoplankton respiration rate.
c_2	0.255	mmol O L ⁻¹	Half-saturation constant for O ₂ respiration by phytoplankton
ν	0.35	d ⁻¹	Maximum per capita zooplankton respiration rate.
c_3	0.255	mmol O L ⁻¹	Half-saturation constant for O ₂ respiration by zooplankton
m	0.03	d ⁻¹	Rate of oxygen loss due to natural depletion.
B	0.055	d ⁻¹	Maximum per capita phytoplankton growth rate.
c_1	0.017	mmol O L ⁻¹	Half-saturation constant for phytoplankton growth.
γ	0.1	mmol O L ⁻¹ d ⁻¹	Intensity of intra-specific competition.
β	0.9	d ⁻¹	Maximum zooplankton predation rate.
H	0.8	mmol N m ⁻³	Half-saturation constant for phytoplankton predation.
σ	0.027	d ⁻¹	Phytoplankton mortality rate.
η	0.75	-	Maximum zooplankton feeding efficiency.
c_4	0.255	mmol O L ⁻¹	Half-saturation constant for zooplankton feeding efficiency.
μ	0.025	d ⁻¹	Zooplankton mortality rate.

Appendix B. Dynamics of the ECC simulation

We analyze the dynamics of the ECC simulation in terms of turbulent energy transfers, mean and eddy-induced circulations and dominant turbulent length scales. Mean quantities refer to the along-shore average, e.g., for the cross-shore velocity u :

$$\langle u(x,z,t) \rangle = L^{-1} \int u(x,y,z,t) dy \quad (B1)$$

where L is the along-shore length of the channel. Perturbations are the departures from this mean: $u' = u - \langle u \rangle$ and $\langle u' \rangle = 0$.

The mean kinetic energy transfer term is $\overline{cke} = -\rho_0 (\langle v_x \rangle \langle u'v' \rangle + \langle v_z \rangle \langle w'v' \rangle + \langle u_x \rangle \langle u'u' \rangle + \langle u_z \rangle \langle w'u' \rangle)$, where ρ_0 is the reference density, v and w the along-shore and vertical velocities and a subscript denotes partial differentiation. The

445 perturbation potential energy transfer term is $\overline{cpe} = -g \langle w'\rho' \rangle$.

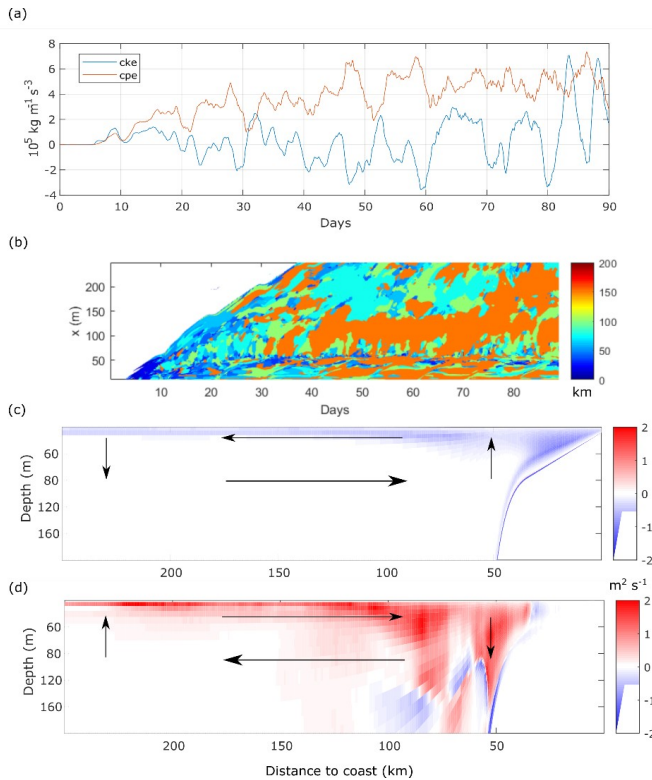
In the ECC case \overline{cpe} remains positive, increasing after the wind intensification part of the wind cycle and decreasing when the wind relaxes (Fig. B1a), while \overline{cke} oscillates between positive and negative values. The mechanism for \overline{cke} growth seems to be the coalescence of disturbances into a single large eddy that is subsequently perturbed by rapidly emerging small scale patterns (Durski and Allen, 2005). Anti-correlation between \overline{cpe} and \overline{cke} is observable at days 35, 47, 53 and 60 (Fig. B1a),

450 suggesting that \overline{cke} evolution is related to nonlinear wave-wave interaction rather than to wave-mean flow interaction (Durski and Allen, 2005). For sustained winds, like the ECC wind cycle with short wind intensification and relaxation periods, the effects of this interaction are significant since the start of the simulations (Durski et al., 2007).

Initially, the surface density peak length-scale l_e , i.e. the most energetic scale, is homogeneous, and l_e is equal to the domain length (Figure B1b).



455 Shortly after the start, small-scale ($O(10\text{km})$) fluctuations appear close to shore, then grow in length and spread offshore. From day 20 onwards, l_e fully develops and ranges from 20 to 160 km across shore, although until day 36 there are still regions where density is rather homogeneous.



460 **Figure B1.** a) Time series of volume averaged perturbation energy source terms; cke source term (green) and cpe source term (blue); volume average in the whole domain. b) Peak wavelength of surface density anomaly alongshore wavenumber spectrum as a function of time and offshore distance. c) Mean stream-function over days 20 to 90. d) Eddy stream-function over days 20 to 90. Mean stratification is shown as black dash-dot contours in panels c and d. Arrows in panels c and d represent a schematic view of the circulation.

465

Offshore the upwelling front (roughly from 50 km) we observe the emergence of two distinct regions in the across-shore direction: a region adjacent to the front where large scale structures are often dominant ($l_e \sim 150 - 160$ km), and further offshore where smaller-scale structures are dominant ($l_e < 100$ km). The cross-shore extent of the first region appears to be related to the excursions in the cke time series (Fig. 3a), judging by the coincidence of the largest fluctuations of cke with the widest swaths of $l_e \sim 150 - 160$ km (days 45, 60, 68 and 80). The second region further offshore seldom exhibits $l_e > 100$ km as it is usually populated by filaments emerging from the front with contrasted density and by vortices resulting from the roll up of filament tips.

470

The wind-induced mean circulation in the $x-z$ plane is $\Psi = -\tau/\rho_0 f$ where τ is the applied wind stress and f the Coriolis parameter. The eddy stream-function is $\psi = (\langle v' b' \rangle - \langle b' z' \rangle - \lambda^2 \langle w' b' \rangle - \langle b' y' \rangle) / (\lambda^2 \langle w' b' \rangle + \langle b' y' \rangle + \langle b' z' \rangle)$, where b is buoyancy and $\lambda = 1000$ is a stretching constant that accounts for the large aspect ratio of oceanic flows (Nagai et al., 2015; Plumb and Ferrari, 2005). The wind-induced mean circulation in the vertical cross-shore plane (Fig. B1c) is stronger at the surface and near the coast and weaker in the interior. A typical upwelling circulation is simulated: Ekman transport moves surface waters offshore and upwards near the coast giving rise to the mean upward tilting of the isopycnals. The eddy induced stream-

475



function (Fig. B1d) represents the component of the flow across the mean isopycnals (Cerovečki et al., 2009; Plumb and
480 Ferrari, 2005), opposes the mean circulation and can surpass it. In agreement with Cerovečki et al. (2009) we find that the
eddy stream-function is stronger at the diabatic surface layer, in a thin layer (up to 20 m depth) with strong shoreward
circulation 100 km offshore, deepening to 150 m at 75 km offshore. There is another strong eddy downwelling cell, on the
shelf-slope transition, that goes down to 160 m depth.

The submesoscale and mesoscale turbulence is sustained by energy transfer from the potential energy field to the turbulent
485 kinetic energy field, through baroclinic conversion (Durski and Allen, 2005; Marchesiello et al., 2003). In agreement with
previous modelling studies (Capet et al., 2008; Durski and Allen, 2005), the global picture is thus that the intermittent wind
bursts act as a recharge for the mean potential energy which is then released to eddy kinetic energy through baroclinic
instability. When the wind decreases, the eddy flux induces a rapid re-stratification of the upper layer (Capet et al., 2008).

Author contributions

490 JHB, VR and VG design the study with input from LR, YM and PH. JHB performed the simulations. JHB, VR and VG
analysed the results and prepared the draft manuscript. All authors critically reviewed, commented and prepared the final
manuscript.

Acknowledgements

This work is part of the TEASAO project, funded by "IDEX attractivity chairs" program from University of Toulouse. JHB
495 acknowledges post-doctoral fellowship financial support from the TEASAO project and CENTEC (University of Lisbon) for
hosting him during his stays. VR acknowledges fruitful discussions with M. Marta-Almeida and travel support from INSU-
CNRS. The MOUTON 2007 campaign was carried out as part of a SHOM (Service Hydrographique et Océanographique de
la Marine) project and we acknowledge the competence and investment of the SHOM technical staff who took part in it.

References

- 500 Adams, K. A., Barth, J. A. and Chan, F.: Temporal variability of near-bottom dissolved oxygen during upwelling off central
Oregon, *Journal of Geophysical Research: Oceans*, 118(10), 4839–4854, doi:10.1002/jgrc.20361, 2013.
- Alvarez-Salgado, X. A., Rosón, G., Pérez, F. F. and Pazos, Y.: Hydrographic variability off the Rías Baixas (NW Spain)
during the upwelling season, *Journal of Geophysical Research*, 98(C8), 14447, doi:10.1029/93JC00458, 1993.
- 505 Behrenfeld, M. J., Halsey Kimberly H and Milligan Allen J: Evolved physiological responses of phytoplankton to their
integrated growth environment, *Philosophical Transactions of the Royal Society B: Biological Sciences*, 363(1504), 2687–
2703, doi:10.1098/rstb.2008.0019, 2008.
- Bettencourt, J. H., López, C., Hernández-García, E., Montes, I., Sudre, J., Dewitte, B., Paulmier, A. and Garçon, V.:
Boundaries of the Peruvian oxygen minimum zone shaped by coherent mesoscale dynamics, *Nature Geoscience*, 8(12), 937–
940, doi:10.1038/ngeo2570, 2015.
- 510 Bettencourt, J. H., Rossi, V., Hernández-García, E., Marta-Almeida, M. and López, C.: Characterization of the Structure and
Cross-Shore Transport Properties of a Coastal Upwelling Filament Using Three-Dimensional Finite-Size Lyapunov
Exponents, *Journal of Geophysical Research: Oceans*, 122(9), 7433–7448, doi:10.1002/2017JC012700, 2017.
- Boyer, T. P., Antonov, J. I., Baranova, O. K., Coleman, C., Garcia, H. E., Grodsky, A., Johnson, D. R., Locarnini, R. A.,
Mishonov, A. V., O'Brien, T. D. and others: *World Ocean Database 2013*, 2013.
- 515 Breitbart, D., Levin, L. A., Oschlies, A., Grégoire, M., Chavez, F. P., Conley, D. J., Garçon, V., Gilbert, D., Gutiérrez, D.,
Isensee, K., Jacinto, G. S., Limburg, K. E., Montes, I., Naqvi, S. W. A., Pitcher, G. C., Rabalais, N. N., Roman, M. R., Rose,
K. A., Seibel, B. A., Telszewski, M., Yasuhara, M. and Zhang, J.: Declining Oxygen in the Global Ocean and Coastal Waters,
Science, 359(6371), eaam7240, doi:10.1126/science.aam7240, 2018.



- 520 Breitburg, D. L., Loher, T., Pacey, C. A. and Gerstein, A.: Varying Effects of Low Dissolved Oxygen on Trophic Interactions in an Estuarine Food Web, *Ecological Monographs*, 67(4), 489–507, doi:10.2307/2963467, 1997.
- Capet, X., McWilliams, J., Molemaker, M. and Shchepetkin, A.: Mesoscale to Submesoscale Transition in the California Current System. Part I: Flow Structure, Eddy Flux, and Observational Tests, *Journal of Physical Oceanography*, 38(1), 29–43, 2008.
- 525 Castaing, B., Gagne, Y. and Hopfinger, E. J.: Velocity Probability Density Functions of High Reynolds Number Turbulence, *Physica D: Nonlinear Phenomena*, 46(2), 177–200, doi:10.1016/0167-2789(90)90035-N, 1990.
- Cerovečki, I., Plumb, R. A. and Heres, W.: Eddy Transport and Mixing in a Wind- and Buoyancy-Driven Jet on the Sphere, *Journal of Physical Oceanography*, 39(5), 1133–1149, doi:10.1175/2008JPO3596.1, 2009.
- Chaigneau, A., Eldin, G. and Dewitte, B.: Eddy Activity in the Four Major Upwelling Systems from Satellite Altimetry (1992–2007), *Progress in Oceanography*, 83(1), 117–123, doi:10.1016/j.pocean.2009.07.012, 2009.
- 530 Charney, J. G.: Geostrophic Turbulence, *Journal of the Atmospheric Sciences*, 28(6), 1087–1095, doi:10.1175/1520-0469(1971)028<1087:GT>2.0.CO;2, 1971.
- Combes, V., Chenillat, F., Lorenzo, E. D., Rivière, P., Ohman, M. D. and Bograd, S. J.: Cross-Shore Transport Variability in the California Current: Ekman Upwelling vs. Eddy Dynamics, *Progress in Oceanography*, 109, 78–89, doi:10.1016/j.pocean.2012.10.001, 2013.
- 535 Debreu, L., Marchesiello, P., Penven, P. and Cambon, G.: Two-Way Nesting in Split-Explicit Ocean Models: Algorithms, Implementation and Validation, *Ocean Modelling*, 49, 1–21, 2012.
- Diaz, R. J. and Rosenberg, R.: Spreading Dead Zones and Consequences for Marine Ecosystems, *Science*, 321(5891), 926–929, doi:10.1126/science.1156401, 2008.
- 540 Durski, S. M. and Allen, J. S.: Finite-Amplitude Evolution of Instabilities Associated with the Coastal Upwelling Front, *Journal of Physical Oceanography*, 35(9), 1606–1628, doi:10.1175/JPO2762.1, 2005.
- Durski, S. M., Allen, J. S., Egbert, G. D. and Samelson, R. M.: Scale Evolution of Finite-Amplitude Instabilities on a Coastal Upwelling Front, *Journal of Physical Oceanography*, 37(4), 837–854, doi:10.1175/JPO2994.1, 2007.
- Feng, Y., DiMarco, S. F. and Jackson, G. A.: Relative role of wind forcing and riverine nutrient input on the extent of hypoxia in the northern Gulf of Mexico, *Geophysical Research Letters*, 39(9), n/a-n/a, doi:10.1029/2012GL051192, 2012.
- 545 Forrest, D. R., Hetland, R. D. and DiMarco, S. F.: Multivariable statistical regression models of the areal extent of hypoxia over the Texas–Louisiana continental shelf, *Environ. Res. Lett.*, 6(4), 045002, doi:10.1088/1748-9326/6/4/045002, 2011.
- Gilly, W. F., Beman, J. M., Litvin, S. Y. and Robison, B. H.: Oceanographic and Biological Effects of Shoaling of the Oxygen Minimum Zone, *Annual Review of Marine Science*, 5(1), 393–420, doi:10.1146/annurev-marine-120710-100849, 2013.
- 550 Gomes, H. do R., Goes, J. I., Matondkar, S. G. P., Buskey, E. J., Basu, S., Parab, S. and Thoppil, P.: Massive outbreaks of *Noctiluca scintillans* blooms in the Arabian Sea due to spread of hypoxia, *Nature Communications*, 5, 4862, doi:10.1038/ncomms5862, 2014.
- 555 Grantham, B. A., Chan, F., Nielsen, K. J., Fox, D. S., Barth, J. A., Huyer, A., Lubchenco, J. and Menge, B. A.: Upwelling-Driven Nearshore Hypoxia Signals Ecosystem and Oceanographic Changes in the Northeast Pacific, *Nature*, 429(6993), nature02605, doi:10.1038/nature02605, 2004.
- Gregg, W. W., Rousseaux, C. S. and Franz, B. A.: Global trends in ocean phytoplankton: a new assessment using revised ocean colour data, *Remote Sensing Letters*, 8(12), 1102–1111, doi:10.1080/2150704X.2017.1354263, 2017.
- 560 Gruber, N., Lachkar, Z., Frenzel, H., Marchesiello, P., Munnich, M., McWilliams, J., Nagai, T. and Plattner, G.: Eddy-Induced Reduction of Biological Production in Eastern Boundary Upwelling Systems, *Nature Geoscience*, 4(11), 787–792, doi:10.1038/NNGEO1273, 2011.
- Gutknecht, E., Dadou, I., Le Vu, B., Cambon, G., Sudre, J., Garçon, V., Machu, E., Rixen, T., Kock, A., Flohr, A., Paulmier, A. and Lavik, G.: Coupled Physical/Biogeochemical Modeling Including O₂-Dependent Processes in the Eastern Boundary Upwelling Systems: Application in the Benguela, *Biogeosciences*, 10(6), 3559–3591, doi:10.5194/bg-10-3559-2013, 2013.



- 565 Hales, B., Karp-Boss, L., Perlin, A. and Wheeler, P. A.: Oxygen Production and Carbon Sequestration in an Upwelling Coastal Margin, *Global Biogeochemical Cycles*, 20(3), GB3001, doi:10.1029/2005GB002517, 2006.
- Harris, G. P.: *Phytoplankton Ecology*, Springer Netherlands, Dordrecht., 1986.
- Head, E. J. H. and Pepin, P.: Spatial and inter-decadal variability in plankton abundance and composition in the Northwest Atlantic (1958–2006), *J Plankton Res*, 32(12), 1633–1648, doi:10.1093/plankt/fbq090, 2010.
- 570 Hernández-Carrasco, I., Rossi, V., Hernández-García, E., Garçon, V. and López, C.: The Reduction of Plankton Biomass Induced by Mesoscale Stirring: A Modeling Study in the Benguela Upwelling, *Deep Sea Research Part I: Oceanographic Research Papers*, 83(Supplement C), 65–80, doi:10.1016/j.dsr.2013.09.003, 2014.
- Large, W. G., McWilliams, J. C. and Doney, S. C.: Oceanic Vertical Mixing: A Review and a Model with a Nonlocal Boundary Layer Parameterization, *Reviews of Geophysics*, 32(4), 363–403, 1994.
- 575 Levin, L. A.: Manifestation, Drivers, and Emergence of Open Ocean Deoxygenation, *Annual Review of Marine Science*, doi:10.1146/annurev-marine-121916-063359, 2018.
- López-Sandoval, D. C., Rodríguez-Ramos, T., Cermeño, P., Sobrino, C. and Marañón, E.: Photosynthesis and respiration in marine phytoplankton: Relationship with cell size, taxonomic affiliation, and growth phase, *Journal of Experimental Marine Biology and Ecology*, 457, 151–159, doi:10.1016/j.jembe.2014.04.013, 2014.
- 580 Lovecchio, E., Gruber, N., Münnich, M. and Lachkar, Z.: On the long-range offshore transport of organic carbon from the Canary Upwelling System to the open North Atlantic, *Biogeosciences*, 14(13), 3337–3369, doi:10.5194/bg-14-3337-2017, 2017.
- Mackey, K. R. M., Paytan, A., Grossman, A. R. and Bailey, S.: A photosynthetic strategy for coping in a high-light, low-nutrient environment, *Limnology and Oceanography*, 53(3), 900–913, doi:10.4319/lo.2008.53.3.0900, 2008.
- 585 Marchesiello, P., McWilliams, J. C. and Shchepetkin, A.: Equilibrium Structure and Dynamics of the California Current System, *J. Phys. Oceanogr.*, 33(4), 753–783, doi:10.1175/1520-0485(2003)33<753:ESADOT>2.0.CO;2, 2003.
- Marta-Almeida, M., Reboreda, R., Rocha, C., Dubert, J., Nolasco, R., Cordeiro, N., Luna, T., Rocha, A., e Silva, J. D. L., Queiroga, H., Peliz, A. and Ruiz-Villarreal, M.: Towards Operational Modeling and Forecasting of the Iberian Shelves Ecosystem, *PLOS ONE*, 7(5), e37343, doi:10.1371/journal.pone.0037343, 2012.
- 590 McClatchie, S., Goericke, R., Cosgrove, R., Auad, G., and Vetter, R.: Oxygen in the Southern California Bight: Multidecadal trends and implications for demersal fisheries, *Geophys. Res. Lett.*, 37, L19602, doi:10.1029/2010GL044497, 2010.
- Miranda, P. M. A., Alves, J. M. R. and Serra, N.: Climate change and upwelling: response of Iberian upwelling to atmospheric forcing in a regional climate scenario, *Clim Dyn*, 40(11–12), 2813–2824, doi:10.1007/s00382-012-1442-9, 2013.
- 595 Moncoiffé, G., Alvarez-Salgado, X. A., Figueiras, F. G. and Savidge, G.: Seasonal and short-time-scale dynamics of microplankton community production and respiration in an inshore upwelling system, *Marine Ecology Progress Series*, 196, 111–126, doi:10.3354/meps196111, 2000.
- Montes, I., Dewitte, B., Gutknecht, E., Paulmier, A., Dadou, I., Oschlies, A. and Garçon, V.: High-Resolution Modeling of the Eastern Tropical Pacific Oxygen Minimum Zone: Sensitivity to the Tropical Oceanic Circulation, *Journal of Geophysical Research: Oceans*, n/a–n/a, doi:10.1002/2014JC009858, 2014.
- 600 Nagai, T., Gruber, N., Frenzel, H., Lachkar, Z., McWilliams, J. C. and Plattner, G.-K.: Dominant Role of Eddies and Filaments in the Offshore Transport of Carbon and Nutrients in the California Current System, *Journal of Geophysical Research: Oceans*, 120(8), 5318–5341, doi:10.1002/2015JC010889, 2015.
- Paulmier, A. and Ruiz-Pino, D.: Oxygen Minimum Zones (OMZs) in the Modern Ocean, *Progress in Oceanography*, 80(3), 113–128, 2009.
- 605 Petrovskii, S., Sekerci, Y. and Venturino, E.: Regime shifts and ecological catastrophes in a model of plankton-oxygen dynamics under the climate change, *Journal of Theoretical Biology*, 424, 91–109, doi:10.1016/j.jtbi.2017.04.018, 2017.
- Plumb, R. A. and Ferrari, R.: Transformed Eulerian-Mean Theory. Part I: Nonquasigeostrophic Theory for Eddies on a Zonal-Mean Flow, *Journal of Physical Oceanography*, 35(2), 165–174, doi:10.1175/JPO-2669.1, 2005.



- 610 Reboreda, R., Cordeiro, N. G. F., Nolasco, R., Castro, C. G., Álvarez-Salgado, X. A., Queiroga, H. and Dubert, J.: Modeling the Seasonal and Interannual Variability (2001–2010) of Chlorophyll-a in the Iberian Margin, *Journal of Sea Research*, 93, 133–149, doi:10.1016/j.seares.2014.04.003, 2014.
- Reboreda, R., Castro, C. G., Álvarez-Salgado, X. A., Nolasco, R., Cordeiro, N. G. F., Queiroga, H. and Dubert, J.: Oxygen in the Iberian Margin: A Modeling Study, *Progress in Oceanography*, 131, 1–20, doi:10.1016/j.pocean.2014.09.005, 2015.
- 615 Renault, L., Deutsch, C., McWilliams, J. C., Frenzel, H., Liang, J.-H. and Colas, F.: Partial Decoupling of Primary Productivity from Upwelling in the California Current System, *Nature Geoscience*, 9(7), 505–508, doi:10.1038/ngeo2722, 2016.
- Roegner, G. C., Needoba, J. A. and Baptista, A. M.: Coastal Upwelling Supplies Oxygen-Depleted Water to the Columbia River Estuary, *PLOS ONE*, 6(4), e18672, doi:10.1371/journal.pone.0018672, 2011.
- 620 Rossi, V., Morel, Y. and Garçon, V.: Effect of the Wind on the Shelf Dynamics: Formation of a Secondary Upwelling along the Continental Margin, *Ocean Modelling*, 31 (3–4), 51–79, 2010.
- Rossi, V., Garçon, V., Tassel, J., Romagnan, J.-B., Stemmann, L., Jourdin, F., Morin, P. and Morel, Y.: Cross-Shelf Variability in the Iberian Peninsula Upwelling System: Impact of a Mesoscale Filament, *Continental Shelf Research*, 59, 97–114, 2013.
- Rykaczewski, R. R., Dunne, J. P., Sydeman, W. J., García-Reyes, M., Black, B. A. and Bograd, S. J.: Poleward displacement of coastal upwelling-favorable winds in the ocean’s eastern boundary currents through the 21st century, *Geophysical Research Letters*, 42(15), 6424–6431, doi:10.1002/2015GL064694, 2015.
- 625 Sekerci, Y. and Petrovskii, S.: Mathematical Modelling of Plankton–Oxygen Dynamics under the Climate Change, *Bulletin of mathematical biology*, 77(12), 2325–2353, 2015.
- Shchepetkin, A. F.: An Adaptive, Courant-Number-Dependent Implicit Scheme for Vertical Advection in Oceanic Modeling, *Ocean Modelling*, 91, 38–69, doi:10.1016/j.ocemod.2015.03.006, 2015.
- 630 Shchepetkin, A. F. and McWilliams, J. C.: The Regional Oceanic Modeling System (ROMS): A Split-Explicit, Free-Surface, Topography-Following-Coordinate Oceanic Model, *Ocean Modelling*, 9(4), 347–404, doi:10.1016/j.ocemod.2004.08.002, 2005.
- Siedlecki, S. A., Banas, N. S., Davis, K. A., Giddings, S., Hickey, B. M., MacCready, P., Connolly, T. and Geier, S.: Seasonal and interannual oxygen variability on the Washington and Oregon continental shelves, *Journal of Geophysical Research: Oceans*, 120(2), 608–633, doi:10.1002/2014JC010254, 2015.
- 635 Sousa, M. C., deCastro, M., Alvarez, I., Gomez-Gesteira, M. and Dias, J. M.: Why coastal upwelling is expected to increase along the western Iberian Peninsula over the next century?, *Science of The Total Environment*, 592, 243–251, doi:10.1016/j.scitotenv.2017.03.046, 2017.
- 640 Torres, R., Barton, E. D., Miller, P. and Fanjul, E.: Spatial patterns of wind and sea surface temperature in the Galician upwelling region, *Journal of Geophysical Research: Oceans*, 108(C4), doi:10.1029/2002JC001361, 2003a.
- Torres, R., Barton, E. D., Miller, P. and Fanjul, E.: Spatial patterns of wind and sea surface temperature in the Galician upwelling region, *Journal of Geophysical Research: Oceans*, 108(C4), doi:10.1029/2002JC001361, 2003b.
- Vaquer-Sunyer, R. and Duarte, C.: Thresholds of Hypoxia for Marine Biodiversity, *Proceedings of the National Academy of Sciences of the United States of America*, 105(40), 15452–15457, doi:10.1073/pnas.0803833105, 2008.
- 645 Vergara, O., Dewitte, B., Montes, I., Garçon, V., Ramos, M., Paulmier, A. and Pizarro, O.: Seasonal Variability of the Oxygen Minimum Zone off Peru in a High-Resolution Regional Coupled Model, *Biogeosciences*, 13(15), 4389–4410, doi:10.5194/bg-13-4389-2016, 2016.
- Wang, D., Gouhier, T. C., Menge, B. A. and Ganguly, A. R.: Intensification and spatial homogenization of coastal upwelling under climate change, *Nature*, 518(7539), 390–394, doi:10.1038/nature14235, 2015.
- 650 Wooster, W. S., Bakun, A. and McLain, D. R.: SEASONAL UPWELLING CYCLE ALONG THE EASTERN BOUNDARY OF THE NORTH ATLANTIC., *J Mar Res*, 34(2), 131–141, 1976.
- Wright, J. J., Konwar, K. M. and Hallam, S. J.: Microbial Ecology of Expanding Oxygen Minimum Zones, *Nature Reviews Microbiology*, doi:10.1038/nrmicro2778, 2012.



655 Zehr, J. P. and Kudela, R. M.: Photosynthesis in the Open Ocean, *Science*, 326(5955), 945–946, doi:10.1126/science.1181277, 2009.

Zhai, L., Platt, T., Tang, C., Sathyendranath, S. and Walne, A.: The response of phytoplankton to climate variability associated with the North Atlantic Oscillation, *Deep Sea Research Part II: Topical Studies in Oceanography*, 93, 159–168, doi:10.1016/j.dsr2.2013.04.009, 2013.

660 Zhang, H., Cheng, W., Chen, Y., Yu, L. and Gong, W.: Controls on the interannual variability of hypoxia in a subtropical embayment and its adjacent waters in the Guangdong coastal upwelling system, northern South China Sea, *Ocean Dynamics*, 68(8), 923–938, doi:10.1007/s10236-018-1168-2, 2018.